Journal of Geophysical Research: Atmospheres

RESEARCH ARTICLE
10.1029/2018JD028824

Properties of Negative Initial Leaders and Lightning Flash Size in a Cluster of Supercells

Dong Zheng[1,2], **Yijun Zhang**[3,4], **and Qing Meng**[1,2]

[1]State Key Laboratory of Severe Weather, Chinese Academy of Meteorological Sciences, Beijing, China, [2]Laboratory of Lightning Physics and Protection Engineering, Chinese Academy of Meteorological Sciences, Beijing, China, [3]Institute of Atmospheric Sciences, Fudan University, Shanghai, China, [4]Shanghai Institute of Pollution Control and Ecological Security, Shanghai, China

Key Points:
- An objective, automated method to identify the negative initial leaders (NILs) and retrieve their parameters is proposed
- Properties of NILs and flash size are counted, while their differences between supercells and *normal* storms are noted
- Charge distribution pattern and density may determine the special characteristics of NILs and flash size in supercells

Correspondence to:
D. Zheng,
zhengdong@cma.gov.cn

Citation:
Zheng, D., Zhang, Y., & Meng, Q. (2018). Properties of negative initial leaders and lightning flash size in a cluster of supercells. *Journal of Geophysical Research: Atmospheres*, *123*, 12,857–12,876. https://doi.org/10.1029/2018JD028824

Received 12 APR 2018
Accepted 6 NOV 2018
Accepted article online 9 NOV 2018
Published online 28 NOV 2018

Author Contributions:
Conceptualization: Dong Zheng
Data curation: Dong Zheng
Formal analysis: Dong Zheng
Funding acquisition: Dong Zheng
Investigation: Dong Zheng
Methodology: Dong Zheng
Resources: Dong Zheng
Supervision: Dong Zheng
Validation: Dong Zheng
Visualization: Dong Zheng
Writing - original draft: Dong Zheng
Writing – review & editing: Dong Zheng

Abstract Properties of negative initial leaders (NILs) and flash size in a cluster of supercells with generally inverted charge structure in Oklahoma on 10–11 May 2010 are examined, primarily using Lightning Mapping Array data. A method to identify NILs from Lightning Mapping Array source is proposed and helps to reveal the multiple NILs properties and their distributions. The NILs in the supercell cluster have smaller speed (median 3-D displacement speed: 0.65×10^5 m/s), relative to the previous reports in *normal* thunderstorms. Furthermore, median NIL speeds initially decrease with increasing height but begin increasing above 12 km. The NILs tend to decelerate during the early stage. The parameters characterizing flash duration and spatial size are also investigated. It is found that they all follow lognormal distributions and the spatial flash size is relatively small on average (median horizontal distance: 5.54 km). Most flashes (83.18%) extend primarily in the horizontal direction. Flash area shows an inverse relationship with flash density at their fast changes during storm evolution. Although large flash initiation density (FID) generally occurs in regions with small flash size, the smallest flash size is nearly not collocated with large FID value. In the regions with large FID, average flash duration roughly increases with increasing FID, while average flash area changes little. We proposed that the pattern of charge pockets and variation of charge density dominated by the strong kinematics are responsible for some new findings about the properties of NIL and flash size in the supercell cluster.

1. Introduction

The development of three-dimensional (3D) lightning location technology has enabled mapping of the propagation processes and flash structure by very low frequency/low frequency or very high frequency location systems (Bitzer et al., 2013; Karunarathne et al., 2013; Rison et al., 1999; Shao et al., 2006; Shi et al., 2017; Thomas et al., 2004; Yoshida et al., 2014; Zhang et al., 2015, 2010), which provide a means for studying flash size and the characteristics of the initial flash leader during the preliminary breakdown (PB) process and for revealing their connections with the parent thunderstorm using large sample data sets.

The PB process is also referred to as the initial breakdown (IB) process and corresponds to the initial stage of a flash after it is initiated. Rison et al. (2016) suggested that many or possibly all flashes are initiated by fast positive breakdown (weak narrow bipolar event-type pulse) associated with positive streamers. It may be then followed by the subsequent changes in the initial electric field associated with weak negative breakdowns (Chapman et al., 2017; Marshall et al., 2014). They commonly enhance the ambient electric field and then guide the occurrence of first IB pulse that used to be regarded as the beginning of a flash (Chapman et al., 2017; Marshall et al., 2014). Most reported initial leaders typically carry negative charge and propagate toward positively charged regions with an average speed on the order of 10^5 m/s (Behnke et al., 2005; Bitzer et al., 2013; Campos & Saba, 2013; Liu & Krehbiel, 1985; Shi et al., 2017; Stolzenburg et al., 2013; Wu et al., 2015). The discontinuous development of the initial leader is sometimes referred to as being *stepwise*. Stolzenburg et al. (2014) proposed that initial leaders might have step patterns that differed from those typical of cloud-to-ground (CG) flashes and were "driven primarily by the large ambient electric field and occur in the absence of a hot channel". The IB pulses associated with initial leaders have been found to be coincident with light bursts observed by high-speed cameras (Campos & Saba, 2013; Stolzenburg et al., 2014, 2013). The step length of initial leaders typically ranges from tens of meters to ~1,000 m (Edens et al., 2014; Rhodes & Krehbiel, 1989; Stolzenburg et al., 2014, 2013; Tran & Rakov, 2016; Wu et al., 2015). Initial leaders develop

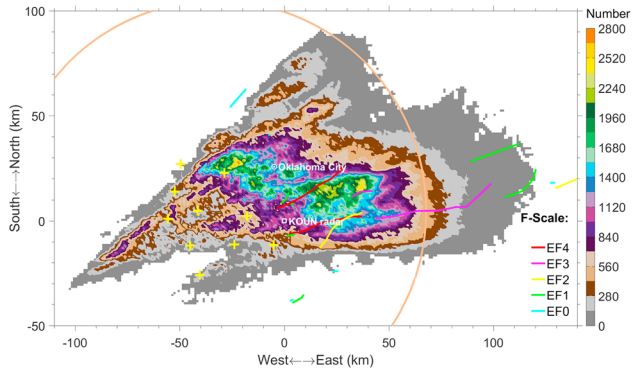

Figure 1. Integrated horizontal source number (shading colors) in the supercell cluster between 2047:33 and 2258:51 UTC (the time of the first volume scan of the KOUN radar with a 0.5° tilt) on 10 May 2010, tornado paths (colored lines described in the legend), and the positions of the OK-LMA sites (yellow crosses) and the KOUN radar (white square). The coordinate origin is located at the position of the KOUN radar that is located in Normal, Oklahoma. The source numbers are for 1 km × 1 km grid boxes. The red-orange curves show parts of a circle enclosing an area within 100 km of the center of the OK-LMA. The tornado paths shown here occurred from 10 to 11 May 2010 (UTC; out of a total of 55 tornadoes documented from 13 storms) and are shown in colors that indicate the EF-scale ratings given to the tornadoes by the National Weather Service.

flash channels into charge regions and precede the propagation caused by breakdown processes in hot conducting channels within the cloud or, occasionally, the leader-return stroke processes forming CG flashes.

Flash size properties have attracted interest in recent years and typically comprise measures of spatial extension and maintenance that include flash duration, channel length, horizontal extent, and flash area, based on the observations of 3-D lightning location systems or satellite-based lightning imaging equipment (Beirle et al., 2014; Bruning & MacGorman, 2013; Lang et al., 2017; López et al., 2017; Peterson, Deierling, et al., 2017; Peterson & Liu, 2013; Peterson, Rudlosky, et al., 2017; Thomas et al., 2013; Zhang et al., 2014; Zhang et al., 2017; Zheng & MacGorman, 2016). Lang et al. (2017) reported the world's largest flash with a horizontal distance of 321 km measured on 20 June 2007 across parts of Oklahoma and the world's longest flash with a duration of 7.74 s measured on 30 August 2012 over parts of southern France. Many studies have suggested that flashes with large average size are more likely to occur in oceanic thunderstorms or weak thunderstorm regions, relative to land thunderstorms or strong convective thunderstorm regions, therefore proposing an inverse relation between flash rate and flash size (Beirle et al., 2014; Bruning et al., 2018; Bruning & MacGorman, 2013; Calhoun et al., 2013; Peterson, Deierling, et al., 2017; Peterson & Liu, 2013; Qie et al., 2003; Zhang et al., 2017; Zheng et al., 2016; Zheng & MacGorman, 2016).

This study investigates the flash activity in a supercell cluster with a general inverted charge structure and aims to answer the following questions. (1) How do the properties of the initial leader and flash size distribute, based on the flash activity during the evolution of the thunderstorm? (2) How can connections among flash initiation, size, and general storm and charge structures be understood? The innovative aspects of this study are as follows: (1) in our analysis of initial leader properties, we include the large number of flashes observed during the evolution of a supercell cluster, which differs from previous studies that either typically use a small number of samples or artificially select suitable examples; (2) most of the observed intracloud flashes have downward propagating negative initial leaders (NILs) resulting from a generally inverted charge structure, whereas previous studies have focused almost exclusively on upward propagating NILs of intracloud flashes associated with a normal charge structure; and (3) the impacts of the storm and charge structures on flash initiation and flash size properties are investigated and discussed.

2. Thunderstorm Processes and Observations

The focus of this study is a cluster of supercells that occurred in Oklahoma from 10 to 11 May 2010 (UTC). It was part of a series of strong storms that occurred at that time, with intense instability characterized by strong low-level shear and large convective available potential energy (2,759 J/kg; Zheng & MacGorman, 2016). Information on this strong storm outbreak and an analysis of the kinematic and microphysical structures of the southern supercell in the cluster can be found in Palmer et al. (2011). Zheng and MacGorman (2016) have investigated this supercell cluster, especially the south supercell, with the concerns being about the spatial correspondence between the positions of flash initiations and kinematic and microphysical structures in the supercell. The evolution of the supercell cluster captured by radar data is described in section 3.1 and shown in Figure 4 of Zheng and MacGorman (2016) and is not reproduced here. In general, the supercell cluster featured merging storms in the south and splitting in the north during its evolution as it moved from west by south to east by north. Because it was difficult to separate the storms in the cluster and the storms ultimately developed into supercells, we studied these storms as a whole. A set of 11 tornadoes (out of a total of 55 tornadoes in 13 storms in this outbreak; see Figure 1), consisting of three EF4-scale, three EF3-scale, one EF2-scale, two EF1-scale, and two EF0-scale events, was documented in the cluster. In addition, 12 hail events with hail diameters from 1.9 to 11.7 cm and 2 strong wind events with velocities greater than 28 m/s were reported.

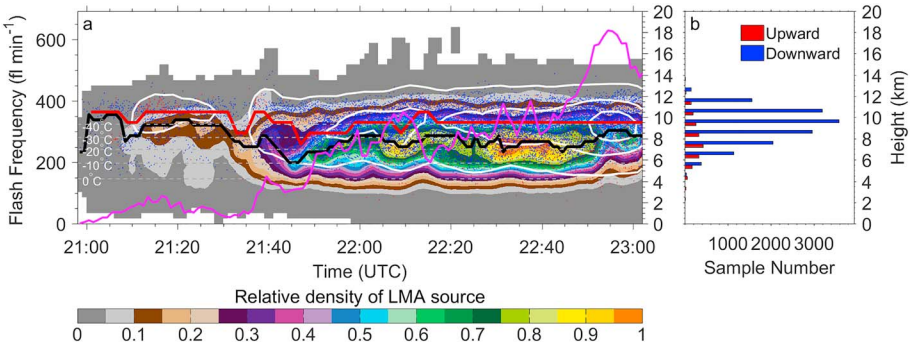

Figure 2. Time-height distribution of flash activity using the same data shown in Figure 1. The shading colors in (a) indicate the relative density of sources as a function of height (right axis) and time (1-min interval and 0.5-km vertical span). The white contour lines in (a) indicate the density of the initial flash positions (the positions of the first sources of a flash) as a function of height and time (2-min interval and 1-km vertical span); the contour values are 10, 50, and 100 moving toward the center. The black and solid red lines in (a) indicate heights with the maximum source density and heights with the most initiation points, respectively. Initiation positions of flashes whose NIL directions can be obtained (see section 3) are shown as red dots for upward NILs and blue dots for downward NILs. Their height distributions are shown in (b). Flash frequencies observed in 1-min intervals are indicated by the solid pink line and the left vertical axis in (a). Levels with environmental temperatures of 0 °C, −10 °C, −20 °C, −30 °C, and −40 °C are shown as gray dashed lines in (a). Temperature values are obtained from a sounding in Norman, Oklahoma, at 2100 UTC on 10 May 2010. Sounding data are provided by the University of Wyoming.

The data used in this study are primarily from flash sources observed by the Oklahoma Lightning Mapping Array (OK-LMA); data from the KOUN polarimetric radar are occasionally referenced. The same data sources were used by Zheng and MacGorman (2016).

The OK-LMA contained 10 available stations (Figure 1) at that time, which located flash breakdown events at frequencies ranging from 60 to 66 MHz by time of arrival technology. Thomas et al. (2004) reported that the source location of LMA had an uncertainty of 6–12 m rms in the horizontal and 20–30 m rms in the vertical. Details about the LMA can be found in Rison et al. (1999), Krehbiel et al. (2000), Thomas et al. (2004), and MacGorman et al. (2008). To ensure data quality, only sources identified by at least seven stations and having chi-square goodness-of-fit values lower than 2 are used (Lund et al., 2009; Thomas et al., 2004). These sources are grouped into flashes following the algorithm used by Zheng and MacGorman (2016) in which a potential flash source must occur within 180 ms of a previous source and within 2 km and 300 ms of any other flash sources. The flash duration must be less than 3 s. The basic principles of this method were introduced by MacGorman et al. (2008), but the parameters have been adapted to the supercells considered here (see Zheng and MacGorman (2016)). Flashes containing no more than 10 sources are not considered.

The S-band KOUN polarimetry radar is located in Norman, Oklahoma (Figure 1). Although the radar data include multiple polarimetric variables, such as differential reflectivity, copular cross-correlation coefficient, and differential phase shift, besides the traditional horizontal polarization Z_{HH}, velocity, and spectrum width, we only use the Z_{HH} in this study. The data were originally observed in 14 elevations. The area of composite reflectivity above 30 dBZ is used in section 6.

From experience, measurements from OK-LMA within a 100-km range (see Figure 1) are thought to be reliable (MacGorman et al., 2008); therefore, we choose storms and flashes between the KOUN radar times of 2047:33 and 2258:51 UTC (the time of the first volume scan with a 0.5° tilt) when the main body of the supercell cluster was located within 100 km of the OK-LMA (although some flashes might be out of this region; see Figure 1). The supercell cluster produced vigorous lightning discharges. The spatial distribution of the sources during this period is shown in Figure 1, where the positions of the OK-LMA sensors, the KOUN radar, and the tornado tracks (all located in the region shown during the outbreak) are also indicated.

A total of 28,872 flashes were recorded in the supercell cluster during the analysis period (this number differs from the 27,297 flashes of Zheng and MacGorman, 2016, because the end of the measurement period in Zheng and MacGorman, 2016, was 2300:00 UTC, whereas here it was 2303:10 UTC, corresponding to the end of last radar volume scan). The variation of flash frequency over time is shown in Figure 2a, which

indicates that our analysis covers the development stage and part of the vigorous stage of the supercell, as the peak flash rate hit more than 600 fl min^{-1}.

The height of the maximum source density (solid black line in Figure 2a) roughly corresponds to the vertical position of the center of the main positively charged region involved in the discharges, because the LMA recorded more breakdown events coming from negative channels that propagated through the positively charged region, than it did the reverse case (Rison et al., 1999; Rust et al., 2005; Thomas et al., 2001). The most flash initiations occurred nearly steadily above the main positively charged center (solid red line in Figure 2a), indicating a general inverted electric structure—that is, upper negative and central positive.

The initial heights of the 16,970 flashes whose NIL directions can be identified (the method will be introduced in section 3) are superimposed in Figure 2a as red dots (upward NILs) and blue dots (downward NILs), and their number distributions with height are shown in Figure 2b. The downward NILs, accounting for ~89% of the flashes considered, had a center initial height between 9 and 10 km (median height of 9.29 km); for upward NILs, the position with the most initial points was between 7 and 8 km (median height of 7.91 km). Below 5 km, although the total number was small, the fraction of upward NILs was greater, which indicated that there might be a small negative charge around the 0 °C level. Therefore, from a macro-perspective, the supercell cluster had a general inverted tripolar charge structure during the analysis period.

The coexistence of initial points belonging to both upward and downward NILs at almost all heights indicates that from a local perspective, the charge regions of the supercell cluster should be not ideally organized into the vertically separated three charge layers. Zheng and MacGorman (2016) determined that the local charge structure in this cluster might be dominated by the pattern of charge pockets suggested by Bruning and MacGorman (2013), under the influence of strong updraft, recycling, entrainment shear, etc. (Browning & Foote, 1976; Klemp & Wilhelmson, 1978; Lemon & Doswell, 1979; Nelson, 1983; Tessendorf et al., 2007; Zheng & MacGorman, 2016). Relative to the horizontally broad and vertically layered charge distribution, the pattern of charge pockets indicates smaller regions of similar polarity and a staggered distribution of regions with different polarity, due to strong convection and turbulent mixing. In this scenario, flash initiation can occur over wide height ranges.

3. Methodology for Quantifying NIL and Flash Size Properties

3.1. Identification and Parameters of NILs

In order to handle the large number of flash samples, an objective, automated method to identify the PB stage and retrieve the NIL parameters from OK-LMA observations is proposed. First, we explicitly define here that the PB process corresponds to the period when a flash is initiated in a strong electric field and its NIL propagates toward the positive charge region. This definition is same to Bitzer et al. (2013), Wu et al. (2015), and Shi et al. (2017). The leaders during the PB process (i.e., initial leaders) are typically thought to have a vertical orientation in the propagation direction. After the PB process, flash channels propagate throughout the region with high charge density (Coleman et al., 2003; Williams et al., 1985) with a primarily horizontal orientation. Furthermore, the method is based on the hypothesis that the NIL is of a single main channel without significant branching. This hypothesis is the basis of many previous studies that calculated NIL parameters (e.g., Behnke et al., 2005; Bitzer et al., 2013; Shao & Krehbiel, 1996; Shi et al., 2017; Wu et al., 2015) and is supported to some extent by Stolzenburg et al. (2014, 2013) who reported the scarcity of branches in initial leaders and regarded it as a distinct difference between initial leaders and typical stepped leaders.

One of the key efforts in calculating NIL properties is to determine the NIL's end time and position. There have been nearly no reports of PB processes lasting more than 100 ms (e.g., Wu et al., 2015; Zhu et al., 2014). Therefore, we first choose sources within the first 100 ms after the initiation of a flash as the preliminary data. We additionally demand that there are at least five source points within the first 30 ms, of which one point must be within 1 km of any other flash source, in order to ensure at least partial spatial continuity and filter the PB process data for quality. Flashes that do not meet these criteria are removed from consideration. Next, the method takes the following steps, which are explained using the example flash case shown in Figure 3.

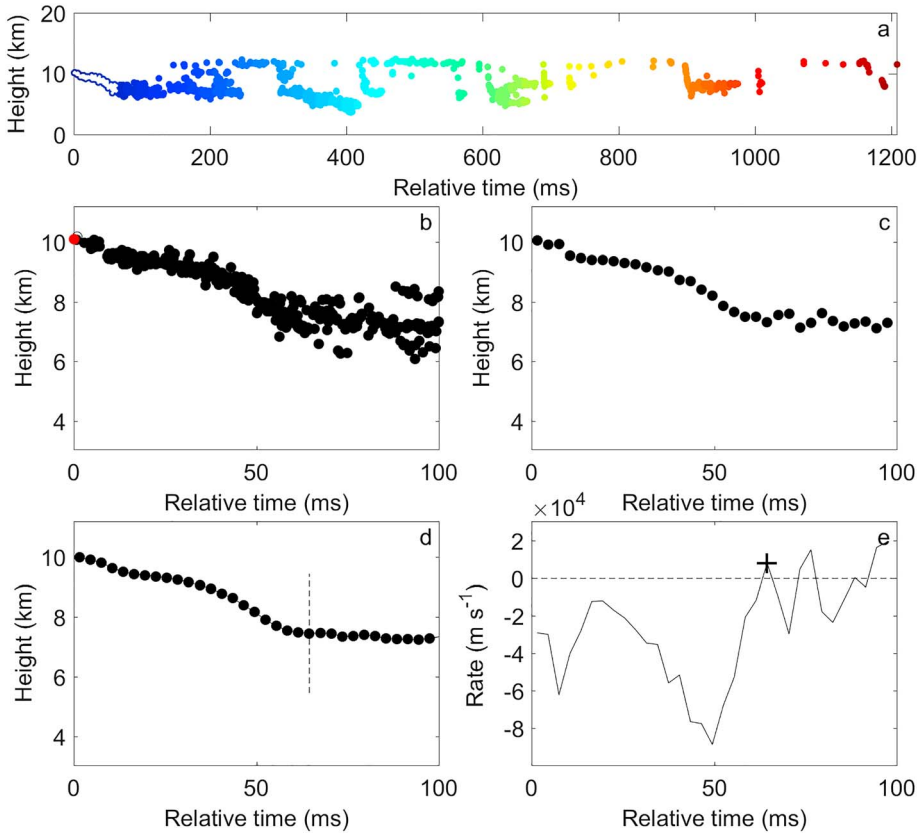

Figure 3. Example of identifying the NIL of a flash occurring at 2140:51.145922327 UTC on 10 May 2010. (a) Time-height pattern of flash source points. (b) First 100 ms of source points in (a); the red dot indicates the position of flash initiation (i.e., the first source). (c) Average height of the source points shown in (b); the average position is determined for 3-ms intervals, and only average heights are shown. (d) Average height after applying the five-point moving average to points shown in (c). (e) Change rate of height of the points shown in (d). The cross in (e) indicates the position where the change rate of height first changes sign. The dashed line in (d) indicates the NIL end time. White dots in (a) indicate source points during the PB process.

1. Determine the initial position of the flash. The first source in a flash is temporarily regarded as the position where the flash is initiated. The chosen 100-ms sources in each flash case and the initial flash position are indicated by a red dot in Figure 3b.
2. Determine the negative leader. The numbers of sources above and below the initial height are each counted for the first 100 ms. Only when one number is more than 2 times larger than the other number will the flash be further considered. The sources with large numbers are believed to be related to negative leaders. Their directions are preliminarily determined to be upward or downward according to the position of these sources relative to the initial height of the flash. In Figure 3b, the solid black dots mark the sources belonging to the negative leader.
3. Obtain the average positions of the negative leader sources in 3-ms time intervals, as shown in Figure 3c (only average heights are shown). If a flash lasts shorter than 3 ms, it will be excluded from the data set.
4. Retrieve the average height of the negative leader sources in 3-ms time intervals using a five-point moving average method, as shown in Figure 3d. In some cases, no sources are located within several continuous 3-ms intervals, which cause the five-point moving average method to fail; these cases are removed.
5. Determine the NIL end time and position. The change rate of the five-point moving average height over time is calculated by investigating the two adjacent points using the following equation:

$$r = \frac{h_2 - h_1}{\Delta t}$$

where r is the change rate of height, h_2 and h_1 are the heights of the two adjacent points, and Δt is the time interval, that is, 3 ms, here. If the change rate of height first reverses its sign (the position marked

by a cross in Figure 3e, it corresponds to the latter one of the two adjacent points) or its absolute value decreases below 10 m/s, we determine that the former point in the two adjacent points corresponds to the NIL end time, as shown by the vertical dashed line in Figure 3d. If the above conditions do not exist within the 100-ms time frame, the corresponding flash is removed from consideration. Furthermore, the direction of the NIL indicated by the sign of the height change rate must be consistent with that obtained in the second step. If not, the flash is removed from consideration.

Parameters describing NIL properties are calculated based on data associated with the average position of the source points, that is, data shown in Figure 3c. They include (1) initial height, (2) duration, (3) vertical displacement (the absolute height difference between the NIL end and start positions), (4) 3-D displacement (the absolute straight line distance between the NIL end and start positions), (5) vertical displacement speed (the vertical displacement divided by the duration), (6) 3-D displacement speed (the 3-D displacement divided by the duration), (7) propagation speed (the 3-D displacement velocity in each neighboring 3-ms time interval), and (8) the angle between the displacement direction and the vertical direction. In some cases, there may be no detected source at the NIL end position; in this situation, parameters (3)–(6) and (8) are not obtained, whereas parameters (1), (2), and (7) are unaffected.

There is a total of 16,970 flashes in the data set whose NIL initial height, propagation direction, and duration can be obtained by the proposed algorithm, including 1,929 upward NILs and 15,041 downward NILs (shown in Figure 2). For the other parameters, excluding propagation speed, the sample numbers are 11,637 total flashes including 1,149 upward NILs and 10,488 downward NILs. For propagation speed, the corresponding number of calculated 3-ms segments are 61,446, 3919 and 57,527, respectively. In the following analysis, we do not distinguish between IC flashes and CG flashes. Zheng and MacGorman (2016) reported an extremely low ratio of CG flashes (1.07%) in this supercell cluster. Although some differences in NIL properties between IC flashes and CG flashes were reported, on the whole, these differences are not enough great to affect results presented here (e.g., Bitzer et al., 2013; Nag & Rakov, 2008; Shi et al., 2017; Weidman & Krider, 1979; Wu et al., 2015).

3.2. Parameters of Flash Size

Flash size here indicates the spatial extent and duration of a flash. We continue to use the example flash shown in Figure 3 to explain the definition of flash size (Figure 4) as it relates to the spatial extent of a flash; the flash duration is equal to the temporal difference between the first and last source in the time sequence of a flash (Figure 3a).

The area of the convex hull of a horizontal plane projection of VHF sources (Figure 4a) roughly indicates the area of the region impacted by a flash. A convex hull is the polygon produced by allowing a band to contract on all the sources of a flash, minimizing the area encompassed by the band. This parameter has been used by Bruning and MacGorman (2013), Bruning and Thomas (2015), Zhang et al. (2017), Zheng and MacGorman (2016), among others and is referred to as flash area in the following text. Similarly, the volume of a 3-D flash convex hull is associated with a polyhedron encompassing all the source points with a minimum volume, as shown in Figure 4d, and is referred to as flash volume in the following text. The horizontal flash distance is indicated by the solid pink line in Figure 4a and describes the maximum distance between any two sources in a flash. The solid pink lines in Figures 4b and 4c both describe the vertical flash distance, which is equal to the difference in height between the highest and lowest sources of a flash. All 28,872 flashes are used to calculate the above parameters.

4. Statistics for NIL Properties

4.1. Distribution of NIL Parameters

Distributions of NIL properties are shown in Figures 5 and 6, and statistics of the parameters are listed in Table 1. The median values of the NIL property parameters were 18.00 ms for duration, 0.63 km for vertical displacement, 1.02 km for 3-D displacement, 0.40×10^5 m/s for vertical displacement speed, 0.65×10^5 m/s for 3-D displacement speed, 1.12×10^5 m/s for propagation speed, and 47.24° for angle. Figure 5 shows that all properties for both upward and downward NILs, except for angle, follow a lognormal distribution, with the bulk of samples having relatively smaller values (the dashed lines in Figures 5a–5f). The angle more closely follows a normal distribution (the dashed line in Figure 5g). The 25th and 75th percentile values are shown

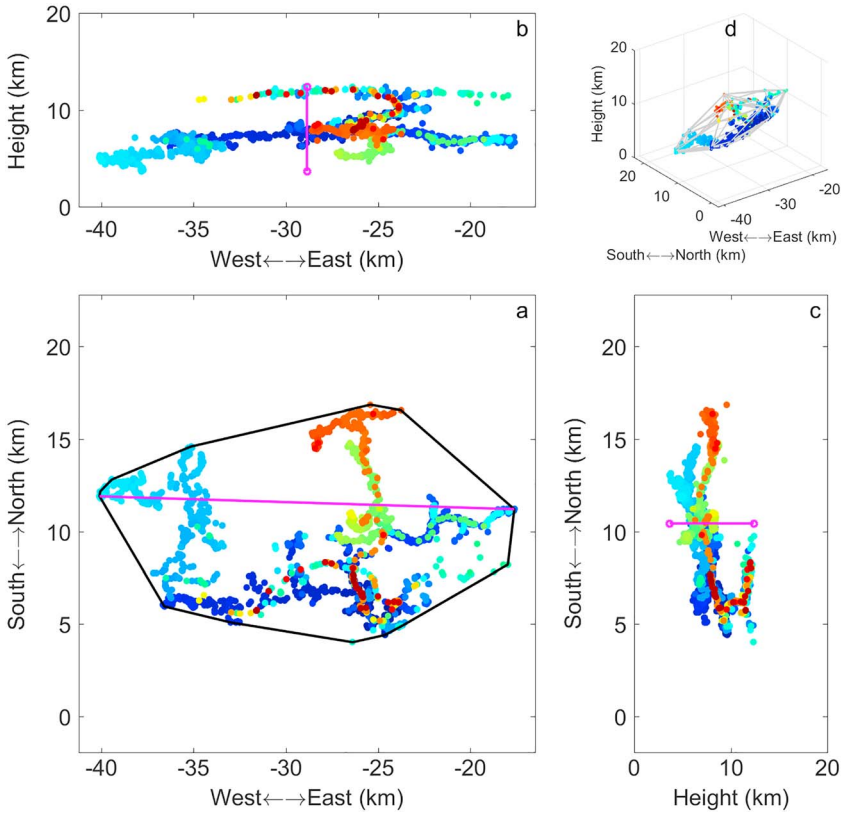

Figure 4. Explanation of the definition of flash size. The flash case is the same as that shown in Figure 3. (a) Horizontal projection of flash source points. (b) Height of flash source points in the west-east direction. (c) Height of flash source points in the north-south direction. (d) Three-dimensional distribution of flash source points. The polygon in (a) is a convex hull of minimum area that contains all the sources. The solid pink line in (a) indicates the longest horizontal flash distance. The solid pink lines in (b) and (c) indicate the maximum vertical distance of the flash. The polyhedron in (d) encompasses all the source points in a 3-D space of minimum volume.

in the box-and-whisker plots in Figure 6. Further analysis indicates that 90% of NILs had a duration shorter than 36 ms, vertical displacement less than 1.90 km, 3-D displacement less than 2.80 km, vertical displacement speed slower than 1.00×10^5 m/s, 3-D displacement speed slower than 1.53×10^5 m/s, and propagation speed slower than 3.07×10^5 m/s. The distributions of upward and downward NILs are each shown in Figures 5 and 6, which reveals no substantial differences between the two groups.

In comparison with NIL speeds reported in other studies, which typically had mean or median values on the order of 10^5 m/s (Behnke et al., 2005; Bitzer et al., 2013; Campos & Saba, 2013; Liu & Krehbiel, 1985; Shi et al., 2017; Stolzenburg et al., 2013; Wu et al., 2015), the NIL speeds in this study are notably smaller. For example, Wu et al. (2015) reported that the vertical speed of upward NILs in 662 positive intracloud flashes over eight thunderstorm days ranged from 0.5 to 17.8×10^5 m/s with an average value of 4.0×10^5 m/s, and an average 3-D displacement speed of 4.3×10^5 m/s. This will be discussed in sections 7.1 and 7.2.

Previous studies have rarely reported other NIL parameters. A reinvestigation of data was reported by Wu et al. (2015), who showed that the peak of the distribution of ratios of horizontal to vertical NIL speed was between 0.4 and 0.6, and reveals that the peak angle of their 662 NILs was between 22° and 31°, whereas our results give values between 40° and 60° for all NILs investigated (Figure 5g). This indicates that the NILs in our study are generally more horizontally oriented than those in Wu et al. (2015). This can be attributed to the pattern of charge pockets discussed in section 2. Under the influence of strong turbulent kinematics in a severe supercell cluster, the charge cores in charge pockets are not as vertically aligned as the stratified and horizontally extending charge regions. Their relatively staggered distribution structure leads to final NIL directions that are more varied and generally more horizontal than those of normal thunderstorms (such as the thunderstorms in Wu et al., 2015).

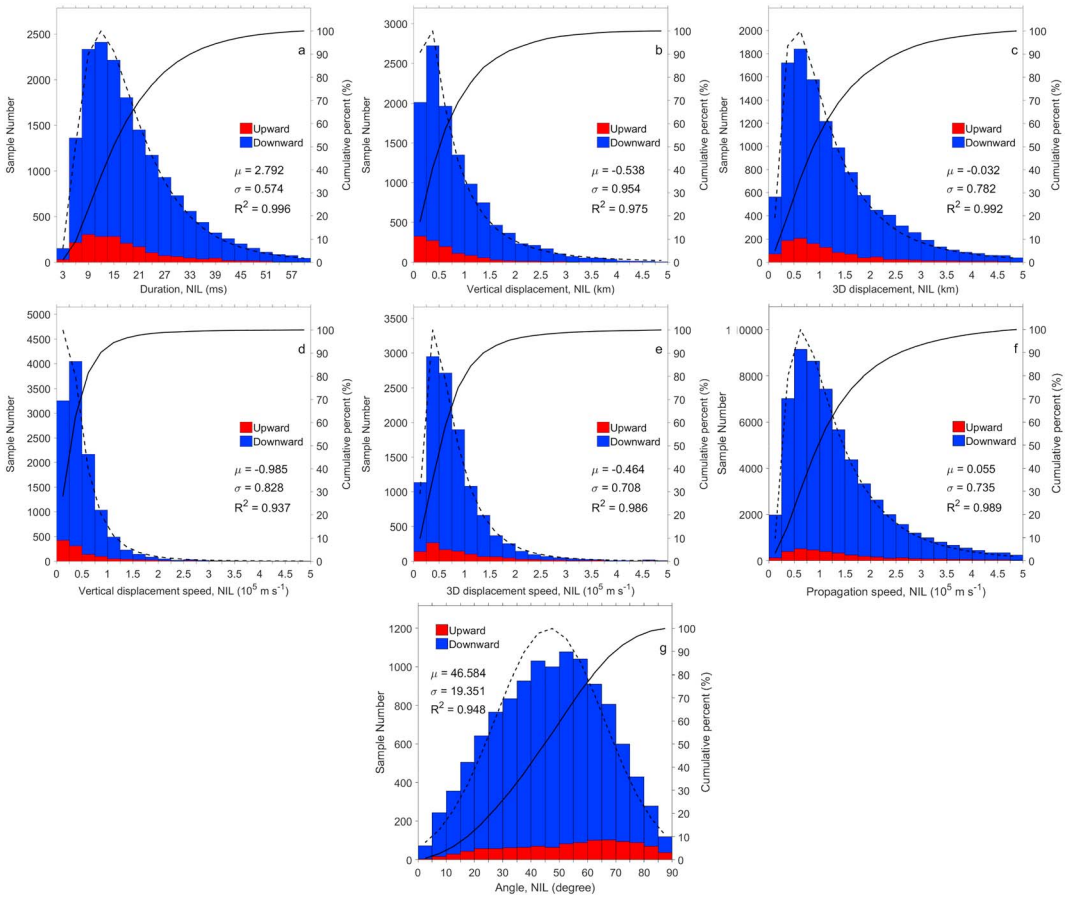

Figure 5. Probability and cumulative distributions of NIL properties including (a) duration, (b) vertical displacement, (c) 3-D displacement, (d) vertical displacement speed, (e) 3-D displacement speed, (f) propagation speed in 3-ms intervals, and (g) angle. The lognormal distributions (a–f) and normal distribution (g) of the NIL properties are described by the dashed lines. These curves are obtained based on the mean (μ) and standard deviation (σ) of the variables (g) or their natural logarithm (a–f). μ and σ are the two parameters in probability density functions of normal distribution and lognormal distribution. R^2 is the goodness of fit of the distribution curves.

4.2. Variation of NIL Properties With Height

Figure 7 shows the distribution of NIL properties with height. At all heights, all parameters are distributed over a wide range. All properties generally decreased with increasing height, except for duration, which showed the opposite trend. Relationships between median values and height are fitted by linear functions (although for some properties, other functions have been shown to result in improved fits). A decrease in NIL speed with height was also reported by Wu et al. (2015). They found that the average speed decreased from 11×10^5 m/s below 4 km to 1.6×10^5 m/s around 11 km. Unexpectedly, NIL propagation speeds reversed their decreasing trend at 12 km (Figure 7e; values for 12 km are calculated using samples between 11.5 and 12.5 km), continuously increasing in median value above 12 km. The 3-D displacement speed also shows this trend above 12 km, which in not evident in the box plot in Figure 7d because only data sets with sample numbers greater than 30 in each height span (1 km) are selected; however, this tendency can be estimated from the scatter points above 12 km in Figure 7d (see also Figure 16). The variation of NIL speed with height will be discussed further in sections 7.1 and 7.2.

4.3. Variation of NIL Propagation Speed With Time

Using propagation speeds over 3-ms time intervals, we calculate NIL acceleration by dividing the difference between adjacent propagation speeds by their time difference (3 ms). Variations of the median acceleration and the sample numbers of upward and downward NILs with the relative time to flash initiation are shown in

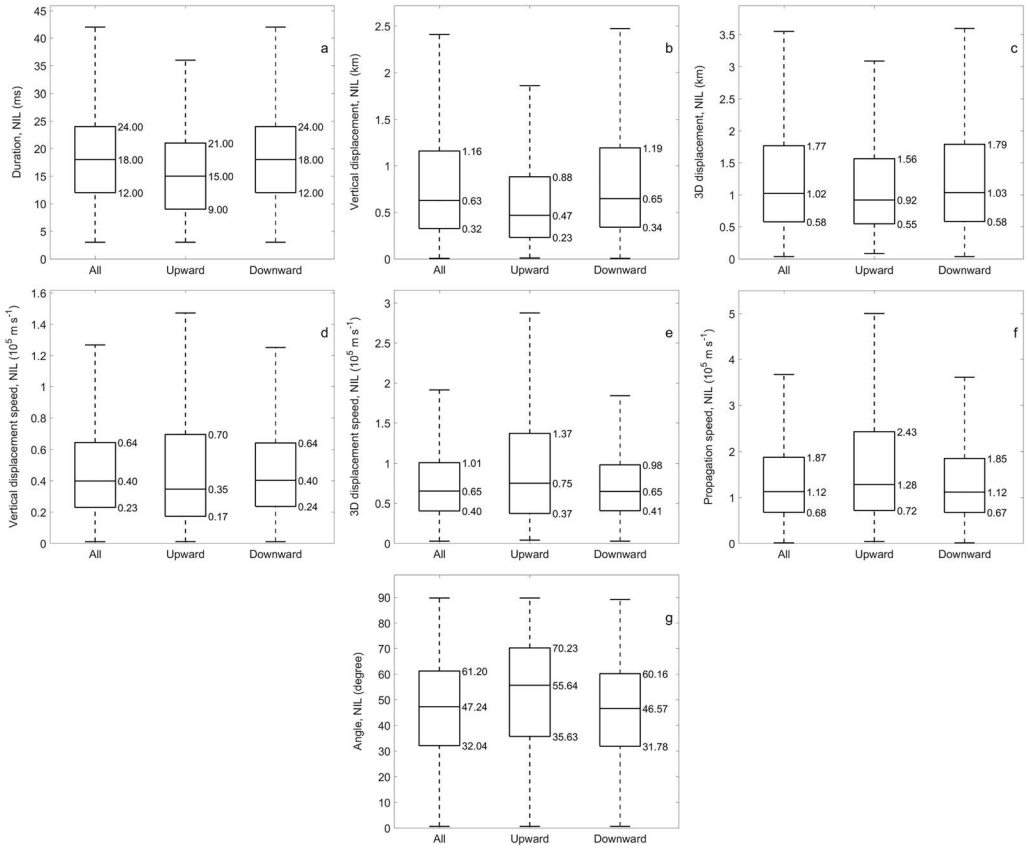

Figure 6. Distributions of the NIL properties in box-and-whisker plots. The sequence of the NIL properties is same to Figure 5. The top, middle, and bottom lines of the boxes represent the 75th percentile (Q3), the median (Q2), and the 25th percentile (Q1). The top and bottom whiskers indicate values of Q3 + 1.5 × (Q3 − Q1) and Q1−1.5 × (Q3 − Q1). Outliers beyond the top and bottom whiskers are not shown.

Figure 8, where the numbers of samples are required to be above 50 and 500 for upward and downward NILs, respectively. This indicates that in the first 30 ms (the analysis of upward NILs ended at 24 ms), NIL propagation speeds first decrease (negative acceleration) and then increase (positive acceleration). Evidently, propagation speeds during 3–6 ms decrease distinctly compared with those during 0–3 ms (indicated by the value at 3 ms along the horizontal axis in Figure 8), for both upward and downward NILs, with their median speeds changing from 1.61×10^5 to 1.23×10^5 m/s and from 1.10×10^5 to 0.99×10^5 m/s, respectively. After the first 6 ms, the median downward NIL acceleration changes to be positive and generally stable before 30 ms, indicating an increasing propagation speed. Upward NILs have small negative median accelerations between 6 and 18 ms, indicating a relatively slow decrease in

Table 1
Statistical Parameters of NIL Properties for the Cluster of Supercells (AM: Arithmetic Mean; GM: Geometric Mean)

		Quantile values				
Parameters	AM	25th	50th	75th	90th	GM
Duration (ms)	19.57	12.00	18.00	24.00	36.00	16.53
Vertical displacement (km)	0.87	0.32	0.63	1.16	1.90	0.59
3-D displacement (km)	1.37	0.58	1.02	1.77	2.80	1.00
Vertical displacement speed (10^5 m/s)	0.51	0.23	0.40	0.64	0.99	0.37
3-D displacement speed (10^5 m/s)	0.84	0.40	0.65	1.01	1.53	0.64
Propagation speed (10^5 m/s)	1.56	0.68	1.12	1.87	13.07	1.12
Angle (degree)	46.58	32.04	47.24	61.20	71.95	41.26

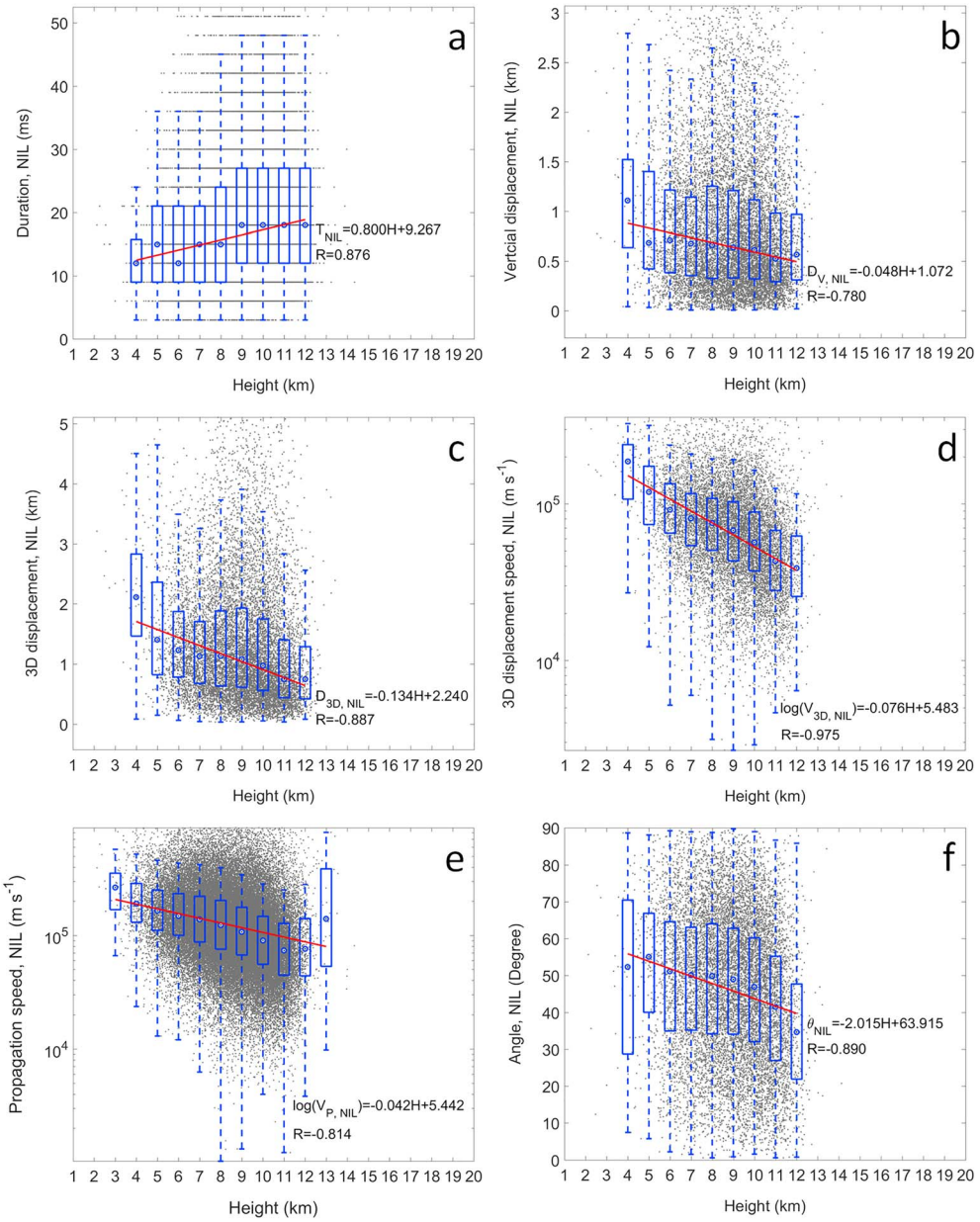

Figure 7. Height distributions of NIL properties: (a) Duration, (b) vertical displacement, (c) 3-D displacement, (d) 3-D displacement speed, (e) propagation speed, and (f) angle. Dark gray dots are NIL properties as a function of height. Overlapped box-and-whisker plots, whose definitions are the same as in Figure 6, but with median values marked by circles, show the distribution pattern of NIL properties for each 1-km span with sample number above 30. Red lines are linear correlations between NIL property median values and height.

propagation speed, which differs from the downward NILs during this period. Between 18 and 24 ms, the propagation speed generally increases, as indicated by the positive median accelerations.

Decreases in propagation speed during the early stage of a NIL were also documented by previous studies. Behnke et al. (2005) reported "the speeds generally decrease with time, from initial values typically between 1 and 3 × 10^5 m/s to final values on the order of or less than 1 × 10^5 m/s" during the first 10–15 ms of discharges in 22 of 24 flashes. Stolzenburg et al. (2013) also observed that two-dimensional (2-D) speed decreased by ~50% over the first 2 ms in seven negative CG flashes. Behnke et al. (2005) suggested that the deceleration of NIL propagation with time might be associated with the decrease or dying out of the preconditioning that supports flash initiation with time and

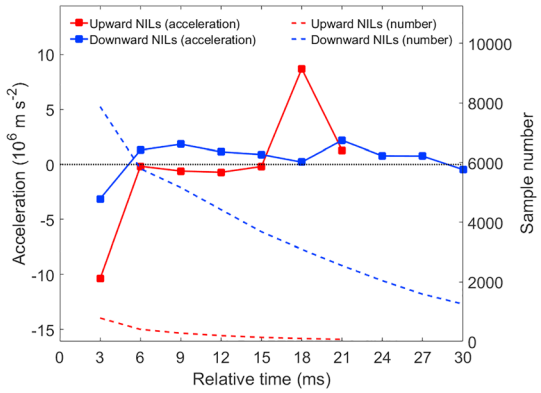

Figure 8. The temporal evolution of median NIL acceleration (ratio of propagation speeds between consecutive 3-ms intervals). Threshold values for the number of samples are 50 and 500 for upward and downward NILs, respectively. Values are labeled at the midpoint of the time intervals; for example, the acceleration value at 3-ms position means the change of propagation speed during the 3–6-ms interval relative to that during the 0–3-ms interval.

distance. In their description, the preconditioning is provided by energetic electron avalanches that are responsible for generating metastable molecules and ions contributing to the fast propagation of the initial leader. But the preconditioning then dissipates with time due to the attachment of ions to water molecules creating cluster molecules, which then attach to particles and decrease in space due to energetic electrons that do not avalanche outside the high-field region but can still produce ionization and metastable states (therefore, the preconditioning effect is small when the NIL travels away from the high field region). After early deceleration, NILs are expected to accelerate due to increases in the electric field at the tip of the NIL as it approaches the opposite-polarity charge core.

5. Statistics for Flash Size Properties

5.1. Distributions of Flash Size Parameters

Figure 9 shows the distributions of flash size parameters, and their statistics are listed in Table 2. All flash size parameters follow

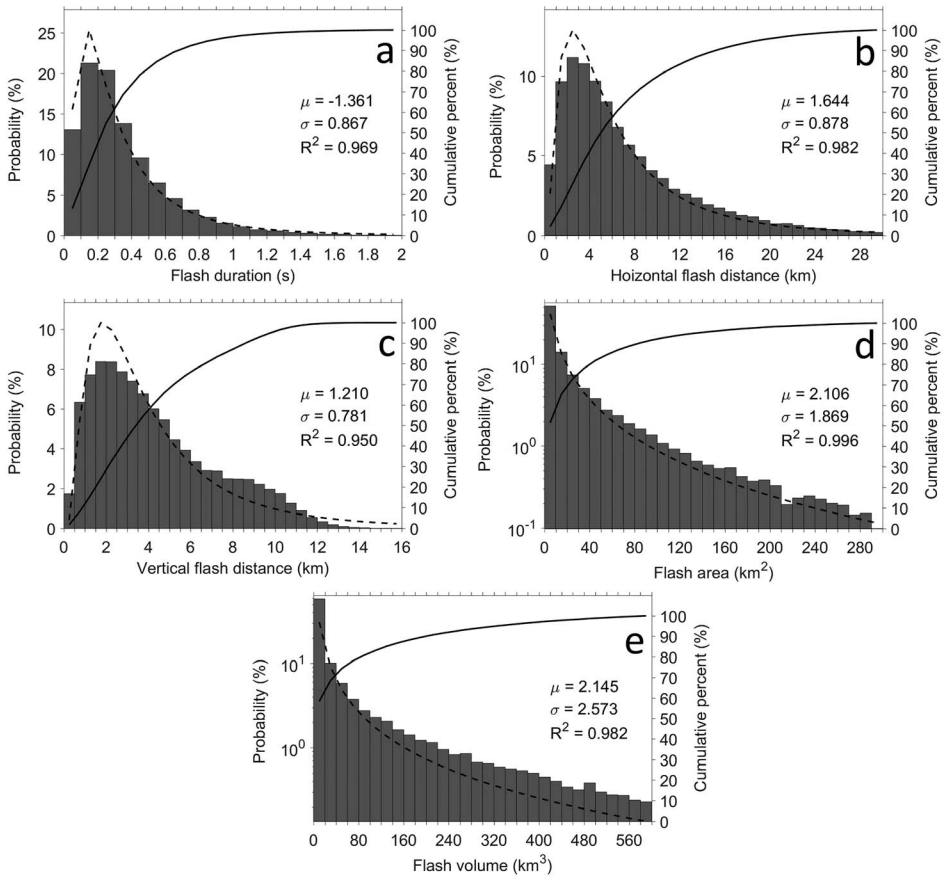

Figure 9. Flash size distributions for (a) flash duration, (b) horizontal flash distance, (c) vertical flash distance, (d) area of the flash convex hull, and (e) volume of the 3-D flash convex hull. Histograms show the probability distribution with the left axes, and lines indicate the cumulative percent distribution with the right axes. The left axes in (d) and (e) use logarithmic scales. The lognormal distribution curves of the flash size parameters, described by the dashed lines, are obtained based on the mean (μ) and standard deviation (σ) of the variables' natural logarithm. R^2 is the goodness of fit of the lognormal distribution curves.

Table 2
Statistics of Flash Size Parameters

Parameters of flash size	AM	Quantile values				GM
		25th	50th	75th	90th	
Flash duration (s)	0.36	0.16	0.27	0.47	0.73	0.26
Horizontal flash distance (km)	7.52	3.00	5.54	10.06	16.20	5.28
Vertical flash distance (km)	4.34	2.05	3.67	6.10	8.85	3.35
Flash area (km^2)	36.16	2.44	9.67	36.22	97.65	8.72
Flash volume (km^3)	145.85	1.88	14.37	94.71	378.48	11.73

lognormal distributions (dashed lines in Figure 9), concentrating a large number of samples in ranges with small values with a long tail toward higher values. Lognormal shapes for flash duration and length were also found by López et al. (2017) based on a sample of 29,000 flashes occurring in multiple storms. The duration, horizontal distance, and vertical distance of the flashes peaked over spans of 0.1–0.5 s, 2–5 km, and 1–3 km, respectively. Flash area and volume displayed the most prominent preference for small values.

Median values of the flash size parameters were 0.27 s for duration, 5.54 km for horizontal distance, 3.67 km for vertical distance, 9.67 km^2 for flash area, and 14.37 km^3 for flash volume, as shown in Table 1. For comparison, Brook and Kitagawa (1960) documented a median flash duration of 0.5 s using the definition that the duration was the time interval between the first burst of pulse activity and the last detectable R- or K-change pulse, and López et al. (2017) reported median (mean) flash durations of 0.35 (0.44) s in summer storms and 0.41 (0.45) s in winter storms with LMA flashes containing more than 50 sources. These values are larger than those found in this study. As for the spatial flash size, López et al. (2017) reported a median (mean) flash length (the length of the major axis of a fitted ellipse, which should be roughly comparable with the horizontal distance) of 10.3 (15.0) km in summer storms and 15.6 (18.4) km in winter storms; their values were much larger than the horizontal distance of 5.54 (7.52) km in this study. Small flash size in this study should be associated with the small-size charge regions in charge-pocket pattern in this supercell cluster due to the strong kinematics.

A comparison between vertical and horizontal flash distance can help describe the basic shape of flashes (horizontally dominated or vertically dominated). Figure 10 presents the flash number distribution in grid boxes of 0.5 km × 0.5 km divided by their horizontal and vertical distances. We found that 83.18% flashes have a horizontally extended shape. In Figure 10, the maximum number densities corresponding to each horizontal distance span are marked by gray dots. A power function was found to produce the best fit for the relationship between the horizontal and vertical flash distances corresponding to the maximum number densities, revealing the most probable horizontal and vertical flash configurations.

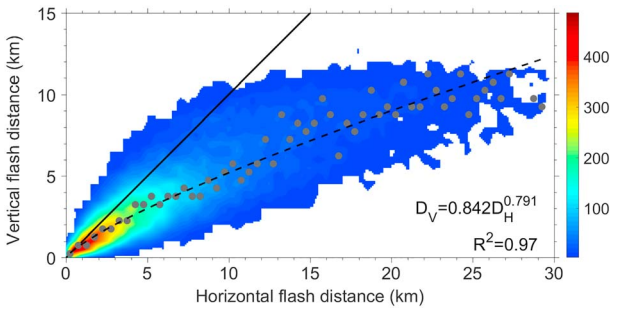

Figure 10. Flash number distribution (shading color) in grid boxes divided by the horizontal and vertical flash distance. The statistical grid box size is 0.5 km × 0.5 km, of which only those with a flash number above 3 are colored. The solid line indicates positions where the horizontal flash distance (D_H) is equal to the vertical flash distance (D_V). Gray dots mark the positions of the grid boxes with the largest number of flashes corresponding to each 0.5-km interval of horizontal extent, where the correlation between horizontal extent and vertical extent is fitted by a power function (dashed line) with the formula shown in the lower right.

5.2. Comparison of Flash Size Parameters

Previous studies typically employed different parameters to describe the flash size, such as the duration and horizontal distance in Lang et al. (2017) and flash area in Bruning and MacGorman (2013), Zhang et al. (2017), and Zheng and MacGorman (2016). To determine whether these differing parameters are comparable, we investigate the relationships between the different flash size properties and present their fitting equations and correlation coefficients in Table 3. Excellent relationships exist between parameters associated with spatial flash size. However, relationships between duration and parameters associated with spatial flash size were less strong. A weak correspondence between duration and spatial size was also reported by Peterson and Liu (2013), who reported a weak linear relationship between the illuminated area and flash duration with a correlation coefficient of 0.39, referring to the

Table 3
Fitting Equations (Lower Left) and Correlation Coefficients (Top Right) Expressing the Relationships Between Various Flash Size Parameters

	Flash duration (T, s),	Horizontal flash distance (D_H, km)	Vertical flash distance (D_V, km)	Flash area (A_{CH}, km^2)	Flash volume (V_{CH}, km^3)
Flash duration (T, s)	–	0.749	0.695	0.771	0.766
Horizontal flash distance (D_H, km)	$D_H = 14.976T^{0.768}$	–	0.853	0.978	0.965
Vertical flash distance (D_V, km)	$D_V = 7.814T^{0.623}$	$D_V = 0.970T^{0.745}$	–	0.878	0.927
Flash area (A_{CH},km^2)	$A_{CH} = 87.293T^{1.697}$	$A_{CH} = 0.266D_{2.097}^{H}$	$A_{CH} = 0.644D_H^{2.154}$	–	0.989
Flash volume (V_{CH}, km^3)	$V_{CH} = 320.001T^{2.43}$	$V_{CH} = 0.081D_H^{2.988}$	$V_{CH} = 0.220D_V^{3.288}$	$V_{CH} = 0.531A_{CH}^{1.429}$	–

flashes observed by Lightning Imaging Sensor. The best relationships are well described by power functions rather than linear functions. In Figure 11, scatterplots and fitted functions for some paired parameters associated with flash size are presented as examples. We further test the relationship between the product of the vertical distance and the area of the flash convex hull (as a rough estimation of the flash volume) and the volume of the 3-D flash convex hull and find a prominent linear correlation, as expected (Figure 11d).

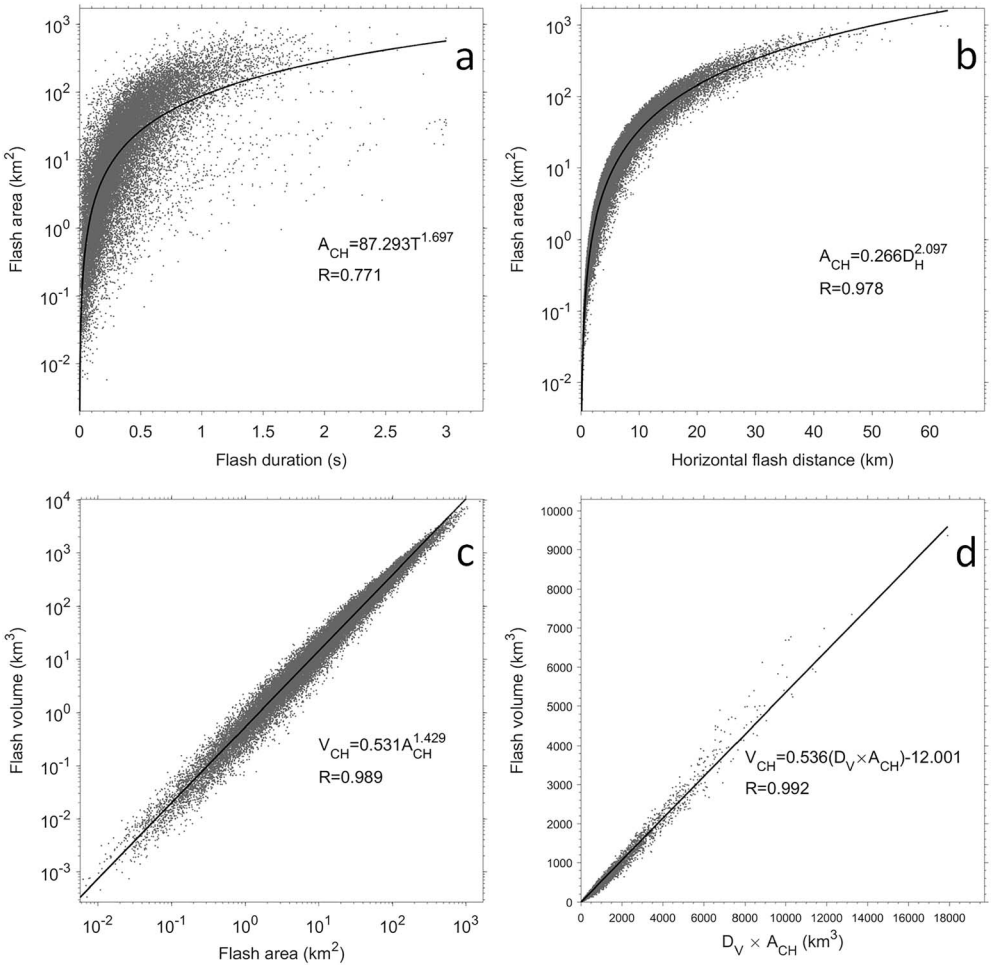

Figure 11. Correlations and their fitting equations for (a) flash duration (T) and area of the flash convex hull (A_{CH}), (b) horizontal flash distance (D_H) and area of the flash convex hull, (c) area of the flash convex hull and volume of the 3-D flash convex hull (V_{CH}), and (d) the product of vertical flash distance and area of the flash convex hull and volume of the 3-D flash convex hull.

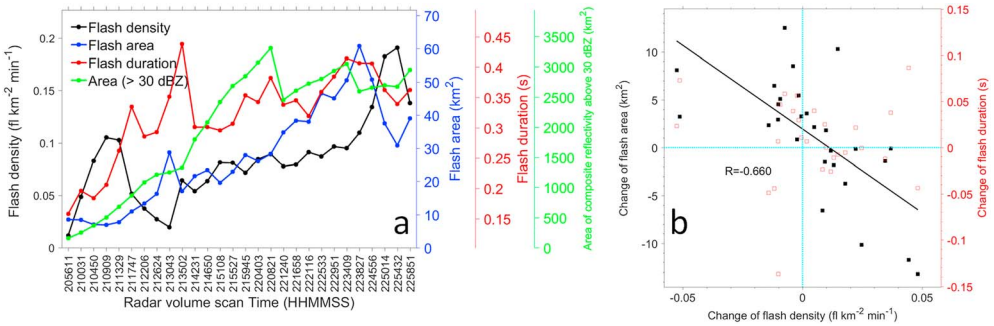

Figure 12. (a) Flash densities, flash areas, flash durations, and composite-reflectivity areas above 30 dBZ during the evolution of the cluster of supercells and (b) correlation of their changes between adjacent radar volume scans. Flash density is defined as flash number over volume scan time interval and area of composite reflectivity above 30 dBZ. Solid black dots in (b) are associated with changes in flash density and flash convex-hull area, and red hollow dots in (b) are associated with changes in flash density and duration.

6. Time-Space Correlation Between Flash Size and Density

Because there are strong correlations between various parameters describing spatial flash size, flash area is used as a proxy of the spatial flash size, along with flash duration.

Figure 12 shows the flash areas, durations, and densities (relative to the radar volume scan time interval and the area of composite reflectivity above 30 dBZ) during the analysis period. In general (i.e., during slow change), the flash size increases with increasing flash density; however, between adjacent radar volume scans (i.e., during fast change), changes in flash area are generally opposite to those of flash density. As shown in Figure 12b, when flash density values change negatively, all (12/12) corresponding flash areas change positively, and when flash density changes positively, ~73% (11/15) of flash areas change negatively. Their change values are linearly fitted with a correlation coefficient of −0.66. Flash duration, however, does not correlate exactly with flash area during fast changes, with a correlation coefficient of only −0.065.

We then investigate the spatial correlation of flash initiation density (FID) with flash size during the evolution of the supercell cluster. FID means the density of initiation positions of flashes in 2 km × 2 km grid box with the unit fl km^{-2} min^{-1}. The flash area in one 2 km × 2 km grid box is counted by averaging the area values of flashes whose channels propagate through this grid box. The results are shown in Figure 13. During the evolution of the supercell cluster, high-density (low-density) flash initiation generally occurred in regions characterized by small (large) flash area or duration, which is directly indicated by that the average flash initiation densities (black lines in Figure 13) are almost always larger than those over regions associated with the top 10% of extreme flash areas or durations (red lines in Figure 13). These results are consistent with previous

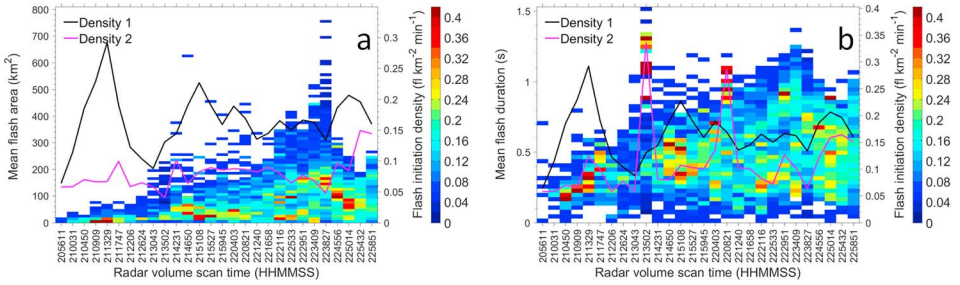

Figure 13. Spatial correlation of flash initiation density (shading colors) to (a) flash area and (b) flash duration during the evolution of the cluster of supercells. Statistical spans are 10 km for flash area and 0.03 s for flash duration. Preliminary data used for this analysis come from spatial counts of flash size and flash initiation density in 2 km × 2 km grid boxes associated with each radar volume scan. Black lines (labeled Density 1) and pink lines (labeled Density 2) associated with the right axes show the temporal evolution of the average flash initiation density for all grid boxes and in grid boxes with the top 10% of flash area (a) and flash duration (b), respectively.

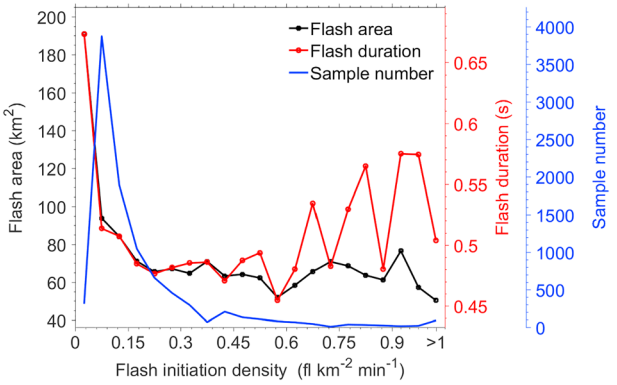

Figure 14. Changes in average flash area and duration with flash initiation density, for 2 km × 2 km grid boxes with flash initiations.

studies that found that small-sized and frequent flashes generally tended to occur in storm regions featuring strong updraft or shear, and large-sized and infrequent flashes generally tended to occur in storm regions with weak kinematics (e.g., Bruning & MacGorman, 2013; Calhoun et al., 2013; MacGorman et al., 2014; Peterson & Liu, 2013; Zhang et al., 2017). However, it should be noted that the smallest flash sizes do not correspond with the large FID values during most evolutionary stages of the supercell cluster, particularly for flash duration, as revealed by investigation of the relative positions of the maximum flash density to the minimum values of flash size in Figure 13.

Figure 14 shows the changes in average flash area and duration with FID for 2 km × 2 km grid boxes with flash initiations. Changes in overall flash size indicate sharp decreases of both flash area and duration with increases in FID in regions with FID lower than 0.25 fl km^{-2} min^{-1}. In other regions, changes in average flash area and duration are both generally slow. Notably, in regions where FID is smaller than ~0.6 fl km^{-2} min^{-1}, the average flash area and duration exhibit nearly the same tendency to decrease; however, in regions with FID above ~0.6 fl km^{-2} min^{-1}, increases in FID is accompanied by increases in average flash duration, although with fluctuations, whereas average flash area changes little.

7. Discussions

7.1. As a Comparison of NIL Speed in Another Supercell

The smaller speeds of the NILs in this supercell cluster than those in *normal* thunderstorms and their increases with height above 12 km should be reported for the first time. In order to determine whether they happened only accidentally in this case, we further investigate the New Mexico (NM) supercell studied by Zhang et al. (2017) based on the NM-LMA observation. The NM supercell was relatively isolated and produced hail with sizes from about 2.24 to 7.62 cm and exhibited flash initiations that varied widely with height and followed patterns of charge pockets (Zhang et al., 2017). Unlike the cluster of supercells explored in this study (referred to as OK supercells in this discussion for clarity), the average height of discharges in the NM supercell underwent a significant rise during the mature stage (Figure 4 in Zhang et al. (2017)), and the flash activity in the adjacent forward anvil was weak (Figure 8 in Zhang et al. (2017)). We use the algorithm described in section 3.1 to calculate NIL parameters of the flashes in the NM supercell, for which 1,518 NILs are selected out of a total of 4,042 flashes. Upward propagating NILs account for ~82% of the samples. It was obtained that the median (mean) vertical speeds were 0.63 (0.82) × 10^5 m/s and the median (mean) 3-D speeds were 0.98 (1.36) × 10^5 m/s, when both upward and downward NILs are included. These values are also generally smaller than those in the previous studies discussed in section 4.1 that primarily focused on normal storms. As for the changes of NIL properties with height, except for NIL angle, all other NIL properties in the NM supercell generally increase or decrease with changes in height, as do those in the OK supercells (Figure 7). The 3-D displacement speed and propagation speed of the NILs in NM supercell are shown in Figure 15. It is obvious that with the increase of height, the median NIL speed in the NM supercell also reverses its tendency from decrease to increase above 12 km for both 3-D displacement speed and propagation speed. Therefore, it is possible that in severe storms, the NIL speed is relatively small and tends to first decrease and then increase with increasing initial height of flashes, with the reverse height being ~12 km.

7.2. Possible Factors Responsible for the Abnormal NIL Speed in Supercells

Wu et al. (2015) attributed their observed decreasing NIL speed with increasing height (their flashes were all initiated below 12 km) to the drop in the breakdown electric field with increasing height, which meant that the ambient electric field for flash propagation tends to be smaller at a higher position than the lower position. Previous studies showed that streamer properties are affected by air density, the electric field, and their physical dimensions (Liu & Pasko, 2004; Qin & Pasko, 2014, 2015); the streamer electron mobility varies positively with electric field and inversely with air density. Therefore, a decreasing electric field with height reduces NIL speed, whereas the decreasing air density with height accelerates the NIL. Thus, the change of

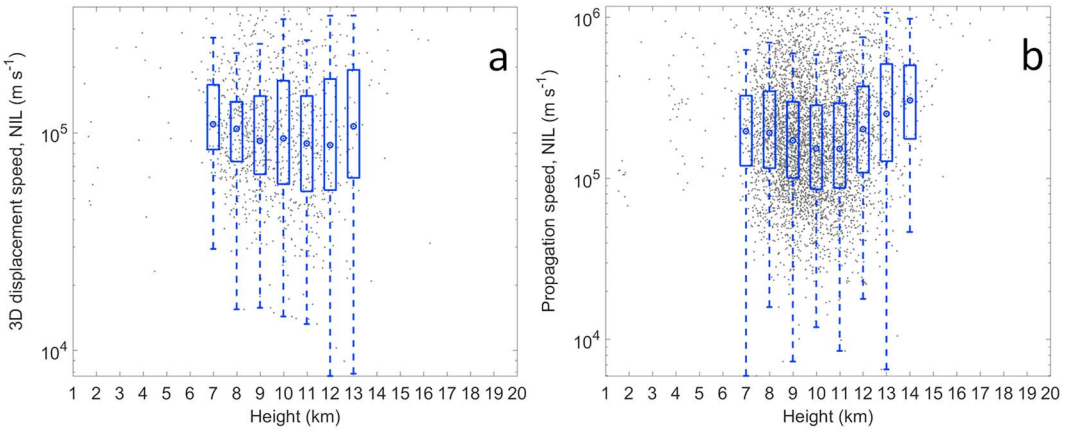

Figure 15. Height distributions of NIL properties including (a) 3-D displacement speed and (b) propagation speed in the New Mexico supercell studied by Zhang et al. (2017).

NIL speed depends on which impact is dominant. From the results, we speculate that the crucial factor impacting the change of NIL speed in height should be the electric field below ~12 km and possibly shift to the air density above ~12 km. Whether the change of NIL speed with height is universal and the factors affecting it warrant further investigation.

As for the smaller NIL speed in OK and NM supercells relative to normal thunderstorm, it may be associated with the charge-pocket patterns in OK and NM supercells. In the pattern of the charge pockets, the chaotic distribution of the small charge regions with opposite polarities can reduce the local ambient electric field and therefore causes a low speed of NIL. If this speculation is correct, it can be expected that the mean NIL speeds in regions characterized by small-sized flashes (those associated with small-charge regions) should be smaller than those in regions characterized by large-sized flashes (those associated with horizontally broad charge regions). In order to test this expectation, mean flash areas in 2 km × 2 km horizontal grid boxes with flash initiations are aggregated for all radar volume scan intervals. Then, using the 25th and 75th percentiles of the flash areas, we divide the NILs of the flashes initiated in the grid boxes into three types: NILs in regions with small-, middle-, and large-sized flashes. In order to avoid the impact of the change of NIL speed with height, we compare the median NIL speed for each type at the same height. Figures 16a and 16b present the results. It is evident that regions with small-sized flashes have the lowest values for median NIL 3-D displacement speed and propagation speed, whereas regions with large-sized flashes have the highest values, consistently at all heights. This trend is also observed for the 25th and 75th percentiles of NIL speed (not shown). Figures 16c and 16d present examples on the NIL speed distributions at 9–10 km, where flash initiations are most frequent. These results support the proposed association of NIL speed with charge pattern.

7.3. Effect of Charge Structure on Flash Size and Flash Initiation Density

Some summarized results in section 6 can be explained by the charge distribution models and their associations with storm kinematics suggested by Bruning and MacGorman (2013). For example, in terms of spatial distribution, the spatial flash size and duration are generally inversely correlated with FID (Figures 13 and 13), which should be due to the charge pockets in regions with strong turbulent kinematics and horizontally broad charge patterns in regions with weak convection. In terms of time evolution, flash area and flash density tend to have an inverse correspondence at their fast changes and consistent tendency at their slow changes. The inverse correspondence should be associated with fast changes in storm kinematics that play crucial roles in shaping the charge distribution (Bruning & MacGorman, 2013). The consistent tendency should be due to the overall growth of the cluster of supercells in the horizontal plane as suggested by the evolution of area of composite reflectivity above 30 dBZ in Figure 12.

Meanwhile, there are some observations that cannot be fully explained by the charge distribution models suggested by Bruning and MacGorman (2013), which are primarily concerned with the scale of the charge

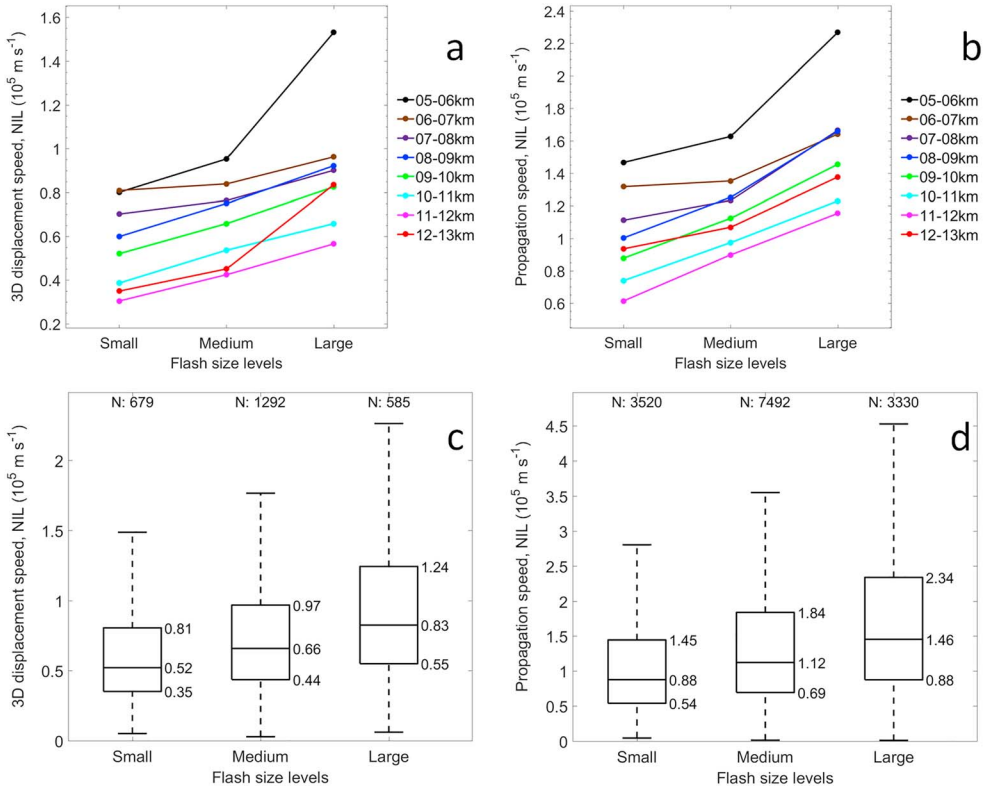

Figure 16. Distributions of NIL speed in regions with small-, middle-, and large-sized flashes: (a) median 3-D speeds and (b) propagation speeds of NILs at different heights and distribution of (c) 3-D speeds and (d) propagation speeds at 9–10 km.

regions. For example, flash duration follows different trends than flash area in regions with large FID (Figures 13 and 14), with weak correlation between the two parameters (Figure 11a and Table 3), and storm areas with smallest flash size generally do not have the largest FID (Figure 13). Here based on the charge distribution models of Bruning and MacGorman (2013), we further consider the possible effects of charge density and quantity on flash initiation and channel propagation and attempt to give a reasonable explanation on the aforementioned phenomena.

As we know, the initial breakdown of flash depends on the ambient electric field that is positively related to the charge quantity. Therefore, although the occurrence of the pattern of charge pockets generally causes high-frequency flash initiations, if the charge regions are too small in size to hold enough charge, the flash initiations between these charge regions may be suppressed. It is why the smallest flash area and duration are nearly not collocated with high-density flash initiation, as shown in Figure 13.

Flash channels tend to propagate toward areas with high density of charge (e.g., Bruning & MacGorman, 2013; Griffiths & Phelps, 1976; MacGorman et al., 2001; Williams et al., 1985). Supposing that the scales of charge regions (valid for the propagation of flash) are constant, the flashes propagating in the charge regions with large-density charge are potential to be tortuous and/or feature more branches and neutralize more charges than those in small-density charge region, which can cause the flashes in large-density charge region to last longer. Meanwhile, the flash areas and distances are limited by the scale of charge regions and expected to change little. Therefore, the flash duration and flash area will change consistently with the scale of the charge regions when the charge densities are relatively small and flash channels are stretched, as the scenario when the FID $<$ ~0.6 fl km^{-2} min^{-1} in Figure 14. When FID $>$ ~0.6 fl km^{-2} min^{-1}, the average flash area keeps relatively stable, meaning that the scale of charge regions changes little on average. The generally increasing flash duration with the increasing FID should be attributed to increasing charge density.

The average convex hull area of flashes can be analogized to the area of charge regions valid for the flash discharges. If using a circle to approximate the flash area, we can get the equivalent diameter of the

charge region. In Figure 14, in the bin where FID $<$0.05 fl km^{-2} min^{-1}, the maximum flash area suggests the average equivalent diameter of charge regions to be approximate 16 km. The average size of charge regions continuously decreases when FID $<$ ~0.25 fl km^{-2} min^{-1}; then it changes little when FID $>$ ~0.25 fl km^{-2} min^{-1} with the estimated average equivalent diameters of the charge regions being approximately between 8 and 10 km. Bryan et al. (2003) reported the turbulent kinetic energy peak was at approximate 10 km in their simulated thunderstorms. It seems that the average scale of charge regions producing the most lightning flashes is same to peak turbulent kinetic scale, which also agree with Bruning and MacGorman (2013) who concluded that the spectrum of flash size was similar to that of turbulent kinematics.

Two limitations of the proposed hypothesis should be noted. First, the values of the thresholds at which the kinematic intensity changes the pattern of the charge regions, and the charge density affects the nature of the flash channels, are uncertain. Numerical simulations may provide a means to estimate these values, as their determination from in situ observations remains difficult. Second, the proposed hypothesis has been developed primarily for supercell storms and may be not suitable for normal storms with generally moderate dynamic processes that lack charge pockets and do not have strong charging processes or large charge densities.

8. Conclusions

In this study, NIL properties and flash size for a cluster of supercells in Oklahoma on 10–11 May 2010 are examined. The cluster of supercells produced active flashes and generally kept an inverted charge structure during the analysis period. We propose a new method to identify NILs using VHF LMA source data and obtain NIL parameters during the evolution of the cluster of supercells, in which ~89% of NILs propagated downward. Flash size is described by the duration, horizontal distance, vertical distance, area, and volume of a flash.

Median values of NIL properties are 18.00 ms for duration, 0.63 km for vertical displacement, 1.02 km for 3-D displacement, 0.40 $\times$ 10^5 m/s for vertical displacement speed, 0.65 $\times$ 10^5 m/s for 3-D displacement speed, 1.12 $\times$ 10^5 m/s for propagation speed, and 47.24° for angle. The angle follows a normal distribution, whereas all other properties follow a lognormal distribution. The NIL speeds in the cluster of supercells are significantly smaller than those reported by other studies that focused on typically normal storms. We suggests an association of slow NIL speed with the pattern of charge pockets in the supercells, which is supported by comparing the 3-D displacement speed and propagation speed of NILs in regions with small-, middle-, and large-sized flashes. It is found that the median, 25th and 75th percentile NIL speeds at different heights all increase with increasing flash size. The median vertical displacement, 3-D displacement, 3-D displacement speed, and propagation speed of the NILs tend to decrease with increasing height. However, this trend reverses around 12 km where median NIL speeds begin to increase with height, which we thought to be associated with the rapid reduction of air density. It is found that the median propagation speed of downward NILs undergoes a significant decrease during the first 6 ms and increases between 6 and 30 ms. The median propagation speed for upward NILs strongly decreases during the first 6 ms, weakly decreases between 6 and 18 ms, and then increases after 18 ms (the statistical analysis period ended at 24 ms).

Median values for the flash size parameters are 0.27 s for duration, 5.54 km for horizontal distance, 3.67 km for vertical distance, 9.67 km^2 for flash area, and 14.37 km^3 for flash volume. All flash size parameters follow lognormal distributions. For 83.18% of the flashes, the horizontal extent exceeds the vertical extent. It is found that parameters describing the spatial flash size are significantly correlated with each other, but their correlations with flash duration are relatively weak. The flash size, flash density, and area of composite reflectivity above 30 dBZ all increase during slow changes of the evolution of the cluster of supercells from an early stage to a vigorous stage, whereas flash area exhibits the opposite trend as flash density during fast changes. Large FID generally tends to occur in regions with small-sized flashes. However, the smallest flash sizes are nearly not collocated with large FIDs, which are suggested to be due to that the flash initiation is suppressed if the charge pockets are too small to hold enough charge. In regions where the FID is smaller than ~0.25 fl km^{-2} min^{-1}, average flash area and duration both sharply decrease with increasing FID, and in regions with FID larger than ~0.25 fl km^{-2} min^{-1}, changes in average flash area are relatively slow (it means that the average scale of charge regions changes little). Furthermore, in regions with FID above ~0.6 fl km^{-2} min^{-1}, average flash duration generally increases, with some fluctuations, whereas average

flash area still changes little. We speculate that if the charge density in charge pockets that keep relatively steady in scale becomes very large (indicated by the increasing FID), the duration of flash propagating in them tends to increase because the potentially neutralizable charge increase, while the spatial flash extent is limited by the charge region scale and changes little. The average equivalent diameter of charge regions producing the most lightning flashes (large FID) is estimated to be between 8 and 10 km, approximately similar to the peak turbulent kinetic scale.

Acknowledgments
This work was supported by the National Key Research and Development Program of China (2017YFC1501503), the National Natural Science Foundation of China (41675005 and 91537209), and the Basic Research Fund of Chinese Academy of Meteorological Sciences (2016Z002). The authors are particularly grateful to Cooperative Institute for Mesoscale Meteorological Studies, University of Oklahoma, which contributes the data on the OK supercells in this study, and New Mexico Institute of Mining and Technology, which contributes that data on the NM supercells referred to in the section of discussion. Our thanks also go to Donald R. MacGorman, Gaopeng Lu, and Zhixiao Zhang who provide important help in collecting and processing the data. The data associated with this paper can be accessed from http://doi.org/10.5281/zenodo.1438115 or from the corresponding author.

References

Behnke, S., Thomas, R., Krehbiel, P., & Rison, W. (2005). Initial leader velocities during intracloud lightning: Possible evidence for a runaway breakdown effect. *Journal of Geophysical Research*, *110*(D10). https://doi.org/10.1029/2004JD005312

Beirle, S., Koshak, W., Blakeslee, R., & Wagner, T. (2014). Global patterns of lightning properties derived by OTD and LIS. *Natural Hazards and Earth System Sciences*, *14*(10), 2715–2726. https://doi.org/10.5194/nhess-14-2715-2014

Bitzer, P. M., Christian, H. J., Stewart, M., Burchfield, J., Podgorny, S., Corredor, D., et al. (2013). Characterization and applications of VLF/LF source locations from lightning using the Huntsville Alabama Marx Meter Array. *Journal of Geophysical Research: Atmospheres*, *118*, 3120–3138. https://doi.org/10.1002/jgrd.50271

Brook, M., & Kitagawa, N. (1960). Some aspects of lightning activity and related meteorological conditions. *Journal of Geophysical Research*, *65*(4), 1203–1210. https://doi.org/10.1029/JZ065i004p01203

Browning, K. A., & Foote, G. B. (1976). Airflow and hail growth in supercell storms and some implications for hail suppression. *Quarterly Journal of the Royal Meteorological Society*, *102*(433), 499–533. https://doi.org/10.1002/qj.49710243303

Bruning, E. C., & MacGorman, D. R. (2013). Theory and observations of controls on lightning flash size spectra. *Journal of the Atmospheric Sciences*, *70*(12), 4012–4029. https://doi.org/10.1175/JAS-D-12-0289.1

Bruning, E. C., Salinas, V., Nixon, C., Berkseth, S., Brothers, M., Mansell, E. R., et al. (2018). The coupling of thunderstorm kinetic and electrical energetics. *XVI International Conference on Atmospheric Electricity*, 17–22 June 2018, Nara city, Nara, Japan.

Bruning, E. C., & Thomas, R. J. (2015). Lightning channel length and flash energy determined from moments of the flash area distribution. *Journal of Geophysical Research: Atmospheres*, *120*, 8925–8940. https://doi.org/10.1002/2015JD023766

Bryan, G. H., Wyngaard, J. C., & Fritsch, J. M. (2003). Resolution requirements for the simulation of deep moist convection. *Monthly Weather Review*, *131*(10), 2394–2416. https://doi.org/10.1175/1520-0493(2003)131<2394:RRFTSO>2.0.CO;2

Calhoun, K. M., MacGorman, D. R., Ziegler, C. L., & Biggerstaff, M. I. (2013). Evolution of lightning activity and storm charge relative to dual-Doppler analysis of a high-precipitation supercell storm. *Monthly Weather Review*, *141*(7), 2199–2223. https://doi.org/10.1175/MWR-D-12-00258.1

Campos, L. Z., & Saba, M. M. F. (2013). Visible channel development during the initial breakdown of a natural negative cloud-to-ground flash. *Geophysical Research Letters*, *40*, 4756–4761. https://doi.org/10.1002/grl.50904

Chapman, R., Marshall, T., Karunarathne, S., & Stolzenburg, M. (2017). Initial electric field changes of lightning flashes in two thunderstorms. *Journal of Geophysical Research: Atmospheres*, *122*, 3718–3732. https://doi.org/10.1002/2016JD025859

Coleman, L. M., Marshall, T. C., stolzenburg, M., Hamlin, T., Krehbiel, P. R., Rison, W., & Thomas, R. J. (2003). Efects of charge and electrostatic potential on lightning propagation. *Journal of Geophysical Research*, *108*(D9). https://doi.org/10.1029/2002JD002718

Edens, H. E., Eack, K. B., Rison, W., & Hunyady, S. J. (2014). Photographic observations of streamers and steps in a cloud-to-air negative leader. *Geophysical Research Letters*, *41*, 1336–1342. https://doi.org/10.1002/2013GL059180

Griffiths, R. F., & Phelps, C. T. (1976). The effects of air pressure and water vapor content on the propagation of positive corona streamers and their implications to lightning initiation. *Quarterly Journal of the Royal Meteorological Society*, *102*(432), 419–426. https://doi.org/10.1002/qj.49710243211

Karunarathne, S., Marshall, T. C., Stolzenburg, M., Karunarathnam, N., Vickers, L. E., Warner, T. A., & Orville, R. E. (2013). Locating initial breakdown pulses using electric field change network. *Journal of Geophysical Research: Atmospheres*, *118*, 7129–7141. https://doi.org/10.1002/jgrd.50441

Klemp, J. B., & Wilhelmson, R. B. (1978). The simulation of three-dimensional convective storm dynamics. *Journal of the Atmospheric Sciences*, *35*(6), 1070–1096. https://doi.org/10.1175/1520-0469(1978)035<1070:TSOTDC>2.0.CO;2

Krehbiel, P. R., Thomas, R. J., Rison, W., Hamlin, T., Harlin, J., & Davis, M. (2000). GPS-based mapping system reveals lightning inside storms. *Eos, Transactions of the American Geophysical Union*, *81*(3), 21–25. https://doi.org/10.1029/00EO00014

Lang, T. J., Pédeboy, S., Rison, W., Cerveny, R. S., Montanya, J., Chauzy, S., MacGorman, D. R., et al. (2017). WMO world record lightning extremes: Longest reported flash distance and longest reported flash duration. *Bulletin of the American Meteorological Society*, *98*(6), 1153–1168. https://doi.org/10.1175/BAMS-D-16-0061.1

Lemon, L. R., & Doswell, C. A. III (1979). Severe thunderstorm evolution and mesocyclone structure as related to tornado genesis. *Monthly Weather Review*, *107*(9), 1184–1197. https://doi.org/10.1175/1520-0493(1979)107<1184:STEAMS>2.0.CO;2

Liu, N. Y., & Pasko, V. P. (2004). Effects of photoionization on propagation and branching of positive and negative streamers in sprites. *Journal of Geophysical Research*, *109*, A04301. https://doi.org/10.1029/2003JA010064

Liu, X.-S., & Krehbiel, P. R. (1985). The initial streamer of intracloud lightning flashes. *Journal of Geophysical Research*, *90*(D4), 6211–6218. https://doi.org/10.1029/JD090iD04p06211

López, J. A., Pineda, N., Montanyà, J., van der Velde, O., Fabró, F., & Romero, D. (2017). Spatio-temporal dimension of lightning flashes based on three-dimensional Lightning Mapping Array. *Atmospheric Research*, *197*, 255–264. https://doi.org/10.1016/j.atmosres.2017.06.030

Lund, N. R., MacGorman, D. R., Schuur, T. J., & Biggerstaff, M. I. (2009). Relationships between lightning location and polarimetric radar signatures in a small mesoscale convective system. *Monthly Weather Review*, *137*(12), 4151–4170. https://doi.org/10.1175/2009MWR2860.1

MacGorman, D. R., Digangi, E., Ziegler, C., Biggerstaff, M. I., Betten, D., &Bruning, E. C. (2014). Flash location, size, and rates relative to the evolving kinematics and microphysics of the 29 May 2012 DC3 supercell storm. Paper presented at AGU Fall Meeting, San Francisco, USA.

MacGorman, D. R., Rust, W. D., Schuur, T. J., Biggerstaff, M. I., Straka, J. M., Ziegler, C. L., Mansell, E. R., et al. (2008). TELEX: The Thunderstorm Electrification and Lightning Experiment. *Bulletin of the American Meteorological Society*, *89*(7), 997–1014. https://doi.org/10.1175/2007BAMS2352.1

MacGorman, D. R., Straka, J. M., & Ziegler, C. L. (2001). A lightning parameterization for numerical cloud models. *Journal of Applied Meteorology*, *40*(3), 459–478. https://doi.org/10.1175/1520-0450(2001)040<0459:ALPFNC>2.0.CO;2

Marshall, T., Stolzenburg, M., Karunarathna, N., & Karunarathne, S. (2014). Electromagnetic activity before initial breakdown pulses of lightning. *Journal of Geophysical Research: Atmospheres*, *119*, 12,558–12,574. https://doi.org/10.1002/2014JD022155

Nag, A., & Rakov, V. A. (2008). Pulse trains that are characteristic of preliminary breakdown in cloud-to-ground lightning but are not followed by return stroke pulses. *Journal of Geophysical Research*, *113*, D01102. https://doi.org/10.1029/2007JD008489

Nelson, S. P. (1983). The influence of storm flow structure on hail growth. *Journal of the Atmospheric Sciences*, *40*, 1965–1983. https://doi.org/10.1175/1520-0469(1983)040<1965:TIOSFS>2.0.CO;2

Palmer, R. D., Bodine, D., Kumjian, M., Cheong, B., Zhang, G., Cao, Q., Bluestein, H. B., et al. (2011). Observations of the 10 May 2010 tornado outbreak using OU-Prime: Potential for new science with high-resolution polarimetric radar. *Bulletin of the American Meteorological Society*, *92*(7), 871–891. https://doi.org/10.1175/2011BAMS3125.1

Peterson, M., Deierling, W., Liu, C., Mach, D., & Kalb, C. (2017). The properties of optical lightning flashes and the clouds they illuminate. *Journal of Geophysical Research: Atmospheres*, *122*, 423–442. https://doi.org/10.1002/2016JD025312

Peterson, M., & Liu, C. (2013). Characteristics of lightning flashes with exceptional illuminated areas, durations, and optical powers and surrounding storm properties in the tropics and inner subtropics. *Journal of Geophysical Research: Atmospheres*, *118*, 11,727–11,740. https://doi.org/10.1002/jgrd.50715

Peterson, M., Rudlosky, S., & Deierling, W. (2017). The evolution and structure of extreme optical lightning flashes. *Journal of Geophysical Research: Atmospheres*, *122*, 13,370–13,386. https://doi.org/10.1002/2017JD026855

Qie, X., Zhou, Y., & Yuan, T. (2003). Global lightning activities and their regional differences observed from the satellite. *Chinese Journal of Geophysics*, *46*(6), 1068–1077. https://doi.org/10.1002/cjg2.437

Qin, J., & Pasko, V. P. (2014). On the propagation of streamers in electrical discharges. *Journal of Physics D: Applied Physics*, *47*(43), 435202. https://doi.org/10.1088/0022-3727/47/43/435202

Qin, J., & Pasko, V. P. (2015). Dynamics of sprite streamers in varying air density. *Geophysical Research Letters*, *42*, 2031–2036. https://doi.org/10.1002/2015GL063269

Rhodes, C., & Krehbiel, P. R. (1989). Interferometric observations of a single stroke cloud-to-ground flash. *Geophysical Research Letters*, *16*(10), 1169–1172. https://doi.org/10.1029/GL016i010p01169

Rison, W., Krehbiel, P. R., Stock, M. G., Edens, H. E., Shao, X.-M., Thomas, R. J., et al. (2016). Observations of narrow bipolar events reveal how lightning is initiated in thunderstorms. *Nature Communications*, *7*, 10721. https://doi.org/10.1034/ncomms10721

Rison, W., Thomas, R. J., Krehbiel, P. R., Hamlin, T., & Harlin, J. (1999). A GPS-based three dimensional lightning mapping system: Initial observations in central New Mexico. *Geophysical Research Letters*, *26*(23), 3573–3576. https://doi.org/10.1029/1999GL010856

Rust, W. D., MacGorman, D. R., Bruning, E. C., Weiss, S. A., Krehbiel, P. R., Thomas, R. J., et al. (2005). Inverted-polarity electrical structures in thunderstorms in the Severe Thunderstorm Electrification and Precipitation Study. *Atmospheric Research*, *76*(1–4), 247–271. https://doi.org/10.1016/j.atmosres.2004.11.029

Shao, X.-M., & Krehbiel, P. R. (1996). The spatial and temporal development of intracloud lightning. *Journal of Geophysical Research*, *101*(D21), 26,641–26,668. https://doi.org/10.1029/96JD01803

Shao, X.-M., Stanley, M., Regan, A., Harlin, J., Pongratz, M., & Stock, M. (2006). Total lightning observations with the new and improved Los Alamos Sferic Array (LASA). *Journal of Atmospheric and Oceanic Technology*, *23*(10), 1273–1288. https://doi.org/10.1175/JTECH1908.1

Shi, D., Zheng, D., Zhang, Y., Zhang, Y., Huang, Z., Lu, W., Chen, S. D., et al. (2017). Low-frequency E-field detection array (LFEDA)—Construction and preliminary results. *Science China Earth Sciences*, *60*(10), 1896–1908. https://doi.org/10.1007/s11430-016-9093-9

Stolzenburg, M., Marshall, T. C., Karunarathne, S., Karunarathna, N., & Orville, R. E. (2014). Leader observations during the initial breakdown stage of a lightning flash. *Journal of Geophysical Research: Atmospheres*, *119*, 12,198–12,221. https://doi.org/10.1002/2014JD021994

Stolzenburg, M., Marshall, T. C., Karunarathne, S., Karunarathna, N., Vickers, L. E., Warner, T. A., et al. (2013). Luminosity of initial breakdown in lightning. *Journal of Geophysical Research: Atmospheres*, *118*, 2918–2937. https://doi.org/10.1002/jgrd.50276

Tessendorf, S. A., Wiens, K. C., & Rutledge, S. A. (2007). Radar and lightning observations of the 3 June 2000 electrically inverted storm from STEPS. *Monthly Weather Review*, *135*(11), 3665–3681. https://doi.org/10.1175/2006MWR1953.1

Thomas, R., Krehbiel, P., Rison, W., Hunyady, S., Winn, W., Hamlin, T., & Harlin, J. (2004). Accuracy of the lightning mapping array. *Journal of Geophysical Research*, *109*, D14207. https://doi.org/10.1029/2004JD004549

Thomas, R. J., Kerhbiel, P. R., Rison, W., &Burning, E. (2013). Lightning flash length estimation from Lightning Mapping Array measurements. Paper presented at 6th conference on the meteorological applications of lightning data, Austin, Texas, USA.

Thomas, R. J., Krehbiel, P. R., Rison, W., Hamlin, T., Harlin, J., & Shown, D. (2001). Observations of VHF source powers radiated by lightning. *Geophysical Research Letters*, *28*(1), 143–146. https://doi.org/10.1029/2000GL011464

Tran, M. D., & Rakov, V. A. (2016). Initiation and propagation of cloud-to-ground lightning observed with a high-speed video camera. *Scientific Reports*, *6*(1), 39521. https://doi.org/10.1038/srep39521

Weidman, C. D., & Krider, E. P. (1979). The radiation field waveforms produced by intracloud lightning discharge processes. *Journal of Geophysical Research*, *84*(C6), 3159−−3164. https://doi.org/10.1029/JC084iC06p03159

Williams, E. R., Cooke, C. M., & Wright, K. A. (1985). Electrical discharge propagation in and around space charge clouds. *Journal of Geophysical Research*, *90*(D4), 6059−−6070. https://doi.org/10.1029/JD090iD04p06059

Wu, T., Yoshida, S., Akiyama, Y., Stock, M., Ushio, T., & Kawasaki, Z. (2015). Preliminary breakdown of intracloud lightning: Initiation altitude, propagation speed, pulse train characteristics, and step length estimation. *Journal of Geophysical Research: Atmospheres*, *120*, 9071–9086. https://doi.org/10.1002/2015JD023546

Yoshida, S., Wu, T., Ushio, T., Kusunoki, K., & Nakamura, Y. (2014). Initial results of LF sensor network for lightning observation and characteristics of lightning emission in LF band. *Journal of Geophysical Research: Atmospheres*, *119*, 12,034–12,051. https://doi.org/10.1002/2014JD022065

Zhang, G., Li, Y., Wang, Y., Zhang, T., Wu, B., & Liu, Y. (2015). Experimental study on location accuracy of a 3D VHF lightning-radiation-source locating network. *Science China Earth Sciences*, *58*(11), 2034–2048. https://doi.org/10.1007/s11430-015-5119-1

Zhang, G., Wang, Y., Qie, X., Zhang, T., Zhao, Y., Li, Y., & Cao, D. (2010). Using lightning locating system based on time-of-arrival technique to study three-dimensional lightning discharge processes. *Science China Earth Sciences*, *53*(4), 591–602. https://doi.org/10.1007/s11430-009-0116-x

Zhang, R., Zhang, G., Li, Y., Wang, Y., Wu, B., Yu, H., & Liu, Y. (2014). Estimate of NO_X production in the lightning channel based on three-dimensional lightning locating system. *Science China Earth Sciences*, *57*(7), 1613–1625. https://doi.org/10.1007/s11430-013-4812-1

Zhang, Z., Zheng, D., Zhang, Y., & Lu, G. (2017). Spatial-temporal characteristics of lightning flash size in a supercell storm. *Atmospheric Research*, *197*, 201–210. https://doi.org/10.1016/j.atmosres.2017.06.029

Zheng, D., & MacGorman, D. R. (2016). Characteristics of flash initiations in a supercell cluster with tornadoes. *Atmospheric Research*, *167*, 249–264. https://doi.org/10.1016/j.atmosres.2015.08.015

Zheng, D., Zhang, Y., Meng, Q., Chen, L., & Dan, J. (2016). Climatological comparison of small- and large-current cloud-to-ground lightning flashes over Southern China. *Journal of Climate*, *29*(8), 2831–2848. https://doi.org/10.1175/JCLI-D-15-0386.1

Zhu, Y., Rakov, V. A., Mallick, S., Tran, M. D., Pilkey, J., & Uman, M. A. (2014). Preliminary breakdown pulse trains in electric field records of negative cloud-to-ground lightning. XV International Conference on Atmospheric Electricity, 15–20 June 2014, Norman, Oklahoma, U.S.A.